POLITECNICO DI TORINO
Repository ISTITUZIONALE

Low-Fidelity Methodology for Rotor Tonal Noise Prediction During Angular Velocity Transients

Original
Low-Fidelity Methodology for Rotor Tonal Noise Prediction During Angular Velocity Transients / Picillo, M., Barbarino, M., Avallone, F.. - In: AIAA JOURNAL. - ISSN 1533-385X. - (2026). [10.2514/1.J066745]

Availability:
This version is available at: 11583/3009831 since: 2026-04-13T11:37:08Z

Publisher:
American Institute of Aeronautics and Astronautics

Published
DOI:10.2514/1.J066745

Terms of use:

This article is made available under terms and conditions as specified in the corresponding bibliographic description in the repository

Publisher copyright
AIAA preprint/submitted version e/o postprint/Author's Accepted Manuscript

(Article begins on next page)

19 November 2026

Low-Fidelity Methodology for Rotor Tonal Noise Prediction During Angular Velocity Transients

Marco Picillo*, Mattia Barbarino**, Francesco Avallone*
*Politecnico di Torino, DIMEAS
**Centro Italiano Ricerche Aerospaziali

Abstract

This work presents a low-fidelity framework for rotor tonal noise prediction during transient variations of rotor angular velocity, developed with the aim of enabling fast and accurate aeroacoustic analyses for electric vertical takeoff and landing vehicles, characterized by distributed-propulsion systems. The approach couples the vortex particle aerodynamic solver FLOWUnsteady with a time domain acoustic solver based on Farassat's 1A formulation of the Ffowcs-Williams and Hawkings equation. The methodology is validated against high-fidelity Lattice–Boltzmann simulations for a two-bladed propeller operating under steady and time-varying angular velocity conditions. The results show that the low-fidelity model accurately computes the aerodynamic loads and tonal noise characteristics predicted by the high-fidelity solver, while requiring orders of magnitude less computational time. During an angular velocity variation, the sound pressure level change is governed by the time-variation of the rotor angular velocity, reaching its maximum where the time derivative of the rotor angular velocity peaks. A low-frequency component emerges along the rotor axis, associated with the axial loading and mean pressure variation induced by thrust changes. The proposed framework demonstrates strong potential for fast noise prediction in transient operating conditions, offering a valuable tool for preliminary design and perception oriented studies for advanced air mobility applications.

Nomenclature

b	=	blade index
C_Q	=	torque coefficient
C_T	=	thrust coefficient
c_∞	=	free-stream speed of sound
D_{prop}	=	propeller diameter
$\boldsymbol{F}_r$	=	blade element force in the radiation direction
i	=	time index
J	=	advance ratio
j	=	blade element index
N_b	=	number of blade elements
n	=	rotor angular velocity (rps)
p'	=	acoustic pressure
R_{tip}	=	propeller tip radius
$\boldsymbol{r}$	=	radiation vector
t	=	observer time
V_∞	=	free-stream velocity
$\boldsymbol{x}$	=	global reference frame
$\boldsymbol{y}$	=	rotor-based reference frame
$\boldsymbol{z}$	=	blade-based reference frame
α	=	inflow angle
η	=	rotor efficiency
ρ_∞	=	free-stream density
τ	=	emission time
τ^*	=	retarded time
Ω	=	rotor angular velocity (rpm)

I. Introduction

ADVANCED Air Mobility (AAM) refers to the use of advanced air transportation systems, including electric Vertical Takeoff and Landing (eVTOL) aircraft and drones, to transport passengers and cargo. AAM encompasses multiple operational concepts, including Urban Air Mobility (UAM), which focuses on missions within urban and suburban areas, and Regional Air Mobility, which targets longer-range operations with larger and faster aircraft. These relatively new concepts have been accelerated, in the recent years, thanks to the technological advance of VTOL vehicles, which are vehicles capable of takeoff and landing in a small space [1] and are mainly driven by distributed propellers. AAM is anticipated to exert a substantial influence on future lifestyles and societal dynamics. Nevertheless, the potential benefits, such as reduced environmental pollution, improved public health, and enhanced transportation efficiency, must contend with critical challenges pertaining to safety, regulatory frameworks, and public acceptance.

In the context of public acceptance, the analysis conducted in [2] indicates that noise constitutes a primary factor influencing societal attitudes toward UAM. Consequently, accurately predicting rotorcraft noise emissions within urban environments, characterized by nonuniform flows [3], gusts [4], and turbulence [5], is of critical importance. In fact, these complex flow conditions lead to nonuniform inflow at the rotor disk, resulting in significant variations in Sound Pressure Level (SPL) and its directivity [6].

In order to predict noise emission, different numerical methods are usually adopted, ranging from high-fidelity to low-fidelity. Both approaches share the same philosophy, based on predicting blade loads using an aerodynamic solver. This information is then translated into an acoustic signal, by an aeroacoustic solver, and finally to noise metrics. The classification of the methods is based on the accuracy of the aerodynamic and acoustic solver used for the simulation. High-fidelity methods adopt Computational Fluid

Dynamics (CFD) methods such as Reynolds-Averaged Navier-Stokes (RANS) [7], Large Eddy Simulations (LES) [8], and Very-Large Eddy Simulations (VLES) [6] to resolve the unsteady aerodynamic field from which the acoustic source terms are derived, while the near to far field propagation in carried out by the Ffowcs Williams and Hawkings equation (FW-H). On the other side, low-fidelity approaches such as Blade Element Momentum Theory (BEMT) [9], Lifting Line Theory [10] and potential flow methods [11] coupled with simplified versions of the FW-H equation such as Hanson's model [12] in the frequency domain and Farassat 1A formulation [13] in the time domain. Various methodologies for the noise prediction in static operations are compared in [14], showing a good agreement with experimental results, but also highlighting the sensitivity to aerodynamic input data for the Farassat's formulations. In [15], a comparison between BEMT, coupled with Hanson's model, with Unsteady Reynolds-Averaged Navier-Stokes, coupled with FW-H analogy, is carried out, showing good agreement, with the low-fidelity approach being orders of magnitude faster with respect to the high-fidelity one.

Noise characteristics from propellers in axial inflow conditions and steady blade loading has been largely studied in the past with the methods presented above. Reference [16] predicted the tonal noise from open rotors solving RANS coupled with the FW-H equation. Reference [8] investigated noise sources of a two-bladed propeller using LES coupled with FW-H equation, while [6] investigated noise directivity using Lattice-Boltzmann/VLES coupled with a FW-H solver for an isolated propeller in axial and nonaxial inflow conditions. Regarding low-fidelity approaches, [17] used BEMT coupled with a far-field formulation of the tonal contribution for the noise prediction of a small rotor in hover, showing good agreement with respect to experimental data. In [18], a low-fidelity methodology based on BEMT and a time domain compact monopole/dipole FW-H analogy coupled with a straight-ray propagation model is adopted to evaluate the acoustic effects of design and operating conditions for a propeller in forward flight. Finally, in [19], a low-order numerical tool is developed, which uses Hanson's theory, for estimating noise emissions from distributed propeller configurations, showing that low-fidelity methods are a good compromise between accuracy and computational efficiency for noise prediction of propellers in different operating conditions.

Although noise prediction for propellers in stationary and axial-inflow conditions has been extensively studied, noise prediction from maneuvering rotorcraft remains a challenging problem. In practice, VTOLs and drones perform complex maneuvers, which are flight conditions characterized by time varying attitude or operating parameters (e.g. rotor angular velocity), as opposed to steady operating conditions such as hover or steady forward flight, where these parameters remain constant in time. Rotorcraft flight, in general, can be described as a sequence of equilibrium states connected by transitional maneuvers, which are marked by nonstationary and aperiodic effects, leading to noise generation mechanisms that significantly differ from the ones in stationary conditions, as reported in [20]. This additional noise, which increases as the duration of the maneuver decreases, is not negligible as it is characterized by a time-dependent directivity significantly different from the stationary case [21]. The majority of studies in the literature employ a quasi-stationary approach, ignoring the transient that occurs when transitioning from one flight condition to another. In [22], the noise of an helicopter transient maneuver is simulated numerically by means of the formulation 1A of Farassat, while in [23], a BEMT solver coupled with an acoustic solver, based on the formulation 1A of Farassat, is used to investigate the effects of a typical eVTOL mission on the noise of an observer fixed with the vehicle.

Despite extensive work on propeller noise under steady operating conditions, the effect of transient angular velocity on tonal noise remains insufficiently explored. In realistic maneuvering flight, rapid variations in rotor speed directly affect both the aerodynamic loading and the resulting acoustic field [24], giving rise to unsteady noise mechanisms that cannot be captured by quasi-steady approaches. Understanding how the noise varies during these short-duration transients is therefore essential for accurate prediction and perception oriented assessment of eVTOL and propeller noise. To address this problem, the present study adopts a low-fidelity framework for predicting the unsteady tonal noise generated during transient angular velocity. The method couples a vortex-particle aerodynamic solver, FLOWUnsteady [25], with a time-domain acoustic solver based on Farassat's 1A formulation. The low-fidelity results are then validated against high-fidelity lattice-Boltzmann simulations through the commercial software 3DS PowerFLOW®.

The paper is organized as follows: Section II describes the computational framework, including both the low and high-fidelity solvers. Sec. III presents the numerical setup and validation against experimental and high-fidelity data. Section IV reports the results for steady and transient operating conditions, highlighting the main physical mechanisms governing the tonal noise generation. Finally, Sec. V summarizes the main conclusions and outlines future developments.

II. Computational Framework

This section describes the two numerical frameworks employed for the simulations. The first couples the vortex-particle aerodynamic solver FLOWUnsteady [25] with an in-house acoustic solver based on Farassat's 1A formulation, whereas the second relies on the commercial package PowerFLOW® [26], which implements the Lattice–Boltzmann method.

A. Low-Fidelity Solver

The low-fidelity (LF) framework combines the aerodynamic solver FLOWUnsteady, based on the Vortex Particle Method, with an in-house time-domain acoustic solver for tonal noise prediction. A schematic representation of the workflow is shown in Fig. 1.

In the *preprocessing* block, the VTOL configuration, including the propeller and wing geometry, and the maneuver specification, which prescribes the time-dependent flight conditions, are defined. These inputs are passed to the *processing* block, consisting of the aerodynamic and acoustic solvers.

FLOWUnsteady adopts a meshless CFD approach that solves the Navier–Stokes equations in velocity–vorticity form. The flow field is discretized by vortex particles, each carrying a compact vorticity distribution represented by a radial basis function. The vorticity evolution of each particle is governed by Eqs. (1) and (2):

$$\frac{\partial \boldsymbol{\Gamma}_p}{\partial t} = (\boldsymbol{\Gamma}_p \cdot \nabla)\boldsymbol{u}(\boldsymbol{x}_p) + 3\boldsymbol{\Gamma}_p \frac{1}{\sigma_p}\frac{\partial \sigma_p}{\partial t} + \frac{1}{\zeta_{\sigma_p}(0)}(-\boldsymbol{M}_p^0 + \boldsymbol{M}_p^1 + \boldsymbol{M}_p^2) - \frac{1}{\zeta_{\sigma_p}(0)}(\boldsymbol{E}_{\text{adv}}(\boldsymbol{x}_p) + \boldsymbol{E}_{\text{str}}(\boldsymbol{x}_p)) \tag{1}$$

$$\frac{\mathrm{d}\boldsymbol{x}_p}{\mathrm{d}t} = \boldsymbol{u}(\boldsymbol{x}_p) \tag{2}$$

Here, $\boldsymbol{\Gamma}_p$ is the vortex strength of the pth particle, $\boldsymbol{x}_p$ its position, and $\boldsymbol{u}$ the local velocity vector. σ_p denotes the core size (filter width),

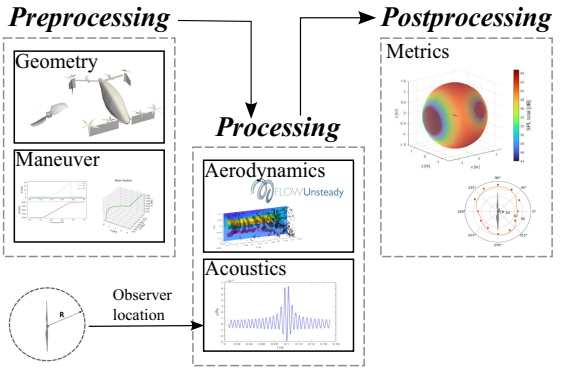


Fig. 1 Low-fidelity simulation framework.

ζ_σ the filter kernel, $\boldsymbol{E}_{\text{adv}}$ and $\boldsymbol{E}_{\text{str}}$ are subfilter-scale vorticity advection and stretching terms, while $\boldsymbol{M}_p$ accounts for particle–particle interactions. Further details are provided in [25].

In FLOWUnsteady, each blade is discretized into elements that incorporate 2D airfoil data (lift and drag coefficients) computed with XFOIL. The aerodynamic forces are reintroduced into the flow field by converting them into equivalent immersed vorticity, according to the Kutta–Joukowski theorem, as in Eq. (3):

$$\Gamma = \frac{cV_{\text{local}}}{2} F_{\text{tip}} F_{\text{hub}} c_\ell \tag{3}$$

where V_{local} is the local velocity at the blade element, c its chord length, and F_{tip} and F_{hub} are the Prandtl tip and hub correction factors, respectively. The accuracy and relatively low computational cost of the method make it suitable for multipropeller aerodynamic analyses [27,28] and aeroacoustic applications [29].

The last component of the *processing* block is the in-house aeroacoustic solver. As illustrated in Fig. 2, the acoustic solver requires as input the load distribution, propeller geometry, and blade kinematics. The propeller kinematics are described by the system of Eq. (4):

$$\begin{cases} \boldsymbol{h}(t_i) = \boldsymbol{h}(t_{i-1}) + \boldsymbol{V}(t_{i-1})\Delta t \\ \boldsymbol{\Theta}(t_i) = \boldsymbol{\Theta}(t_{i-1}) + \boldsymbol{\Omega}(t_{i-1})\Delta t \\ \hat{\boldsymbol{n}}(t_i; j, b) = \boldsymbol{R}_{\text{GR}}(t_i)\hat{\boldsymbol{n}}_0 \\ \hat{\boldsymbol{t}}(t_i; j, b) = \boldsymbol{R}_{\text{GR}}(t_i)\hat{\boldsymbol{t}}_0 \\ \hat{\boldsymbol{r}}(t_i; j, b) = \boldsymbol{R}_{\text{GR}}(t_i)\hat{\boldsymbol{r}}_0 \\ \boldsymbol{y}(t_i; j, b) = \boldsymbol{h}(t_i) + \boldsymbol{R}_{\text{GR}}(t_i)\boldsymbol{z}(t_i; j, b) \end{cases} \tag{4}$$

The first two relations compute the translational and rotational motion of the blade reference frame ($\boldsymbol{Z}$), where $\boldsymbol{h}(t_i)$ and $\boldsymbol{\Theta}(t_i)$ denote the hub position and rotation angle, updated from their previous values using the translational velocity $\boldsymbol{V}(t_{i-1})$ and angular velocity $\boldsymbol{\Omega}(t_{i-1})$. The subsequent equations describe the transformation of the local blade coordinate system through the global–rotor rotation matrix $\boldsymbol{R}_{\text{GR}}(t_i)$, which maps the initial unit vectors $\hat{\boldsymbol{n}}_0$, $\hat{\boldsymbol{t}}_0$, and $\hat{\boldsymbol{r}}_0$ (normal, tangential, and radial directions, respectively) into their instantaneous orientations. Finally, the position of each blade element $\boldsymbol{y}(t_i; j, b)$ is obtained as the sum of the hub position $\boldsymbol{h}(t_i)$ and the rotated local coordinates $\boldsymbol{z}(t_i; j, b)$. The adopted reference frames are illustrated in Fig. 3.

Solving Eq. (4) for each blade element j, blade b, and time step i provides a consistent description of the blade kinematics in both translational and rotational motion, which is essential for the time-history evaluation of the aeroacoustic source terms.

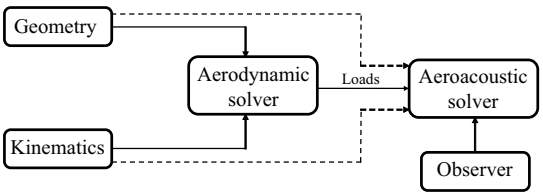


Fig. 2 Processing block.

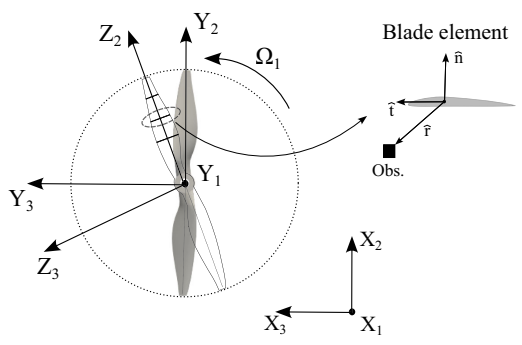


Fig. 3 Rotor sketch and reference frames.

The aeroacoustic solver is based on the time-domain FW–H acoustic analogy in its retarded-time formulation. The FW–H equation decomposes the acoustic field into quadrupole, dipole, and monopole source terms as shown in Eq. (5):

$$\begin{aligned} \rho'(\boldsymbol{x}, t)c_\infty^2 = {} & \frac{\partial^2}{\partial x_i \partial x_j} \int_{V_0} \left[\frac{T_{ij}}{4\pi r|1 - M_r|}\right]_{\tau=\tau^*} \mathrm{d}V(\boldsymbol{z}) \\ & - \frac{\partial}{\partial x_i} \int_{S_0} \left[\frac{p_{ij} n_j}{4\pi r|1 - M_r|}\right]_{\tau=\tau^*} \mathrm{d}S(\boldsymbol{z}) \\ & + \frac{\partial}{\partial t} \int_{S_0} \left[\frac{\rho_\infty V_j n_j}{4\pi r|1 - M_r|}\right]_{\tau=\tau^*} \mathrm{d}S(\boldsymbol{z}) \end{aligned} \tag{5}$$

Here, T_{ij} is the Lighthill stress tensor, c_∞ the speed of sound, $\boldsymbol{z}$ the source position, $\boldsymbol{x}$ the observer position, S_0 the blade surface, V_0 its enclosed volume, $\boldsymbol{r}$ the relative distance vector between observer and source, and M_r the relative Mach number. All quantities are evaluated at the retarded time τ^*, defined implicitly by Eq. (6):

$$t - \tau - \frac{|\boldsymbol{x} - \boldsymbol{y}(\tau)|}{c_\infty} = 0 \tag{6}$$

In the LF framework, only the monopole and dipole terms (thickness and loading noise) are computed. The loading noise is evaluated using Farassat's 1A formulation [22], reported in Eq. (7), while the thickness noise follows the far-field approximation as proposed in [30] (pp. 415), and described in Eq. (8):

$$\begin{aligned} 4\pi p'_L(\boldsymbol{x}, t) = {} & \frac{1}{c_\infty} \int_{f=0} \left[\frac{\dot{\ell}_r}{r|1 - M_r|^2}\right]_{\tau=\tau^*} \mathrm{d}S \\ & + \int_{f=0} \left[\frac{\ell_r - \ell_M}{r^2|1 - M_r|^2}\right]_{\tau=\tau^*} \mathrm{d}S \\ & + \frac{1}{c_\infty} \int_{f=0} \left[\frac{\ell_r(r\dot{M}_r + c_\infty M_r - cM^2)}{r^2|1 - M_r|^3}\right]_{\tau=\tau^*} \mathrm{d}S \end{aligned} \tag{7}$$

$$4\pi p'_T(\boldsymbol{x}, t) \approx \int_{f=0} \left[\frac{\rho_\infty}{r} \frac{\ddot{M}_r}{|1 - M_r|^4} + \frac{3\dot{M}_r^2}{|1 - M_r|^5}\right]_{\tau=\tau^*} \mathrm{d}V \tag{8}$$

In these equations, ℓ_r is the dot product between the surface pressure vector and the radiation direction $\hat{\boldsymbol{r}}$, while ℓ_M is its projection along the surface velocity vector normalized by the speed of sound. The overdot indicates differentiation with respect to the emission time. Thinking in terms of forces, the contribution of each blade element j is $\boldsymbol{F} = l\Delta S$ in the global reference frame and $\boldsymbol{F}_r = l_r \Delta S$ in the radiation direction. The derivative of the force in the radiation direction can be written as

$$\dot{F}_r = \boldsymbol{F} \cdot \dot{\hat{\boldsymbol{r}}} + \dot{\boldsymbol{F}} \cdot \hat{\boldsymbol{r}} \tag{9}$$

The integrands in Eqs. (7) and (8) are evaluated for each blade element at the corresponding retarded time, yielding the pressure signal as a function of observer time for the prescribed rotor motion, as illustrated in Fig. 4.

B. High-Fidelity Solver

The flow is computed with 3DS PowerFLOW® 6–2024, which employs a Lattice-Boltzmann framework coupled with a wall-modeled VLES-turbulence treatment [31]. In this approach, the solver advances the Boltzmann equation for the particle distribution $f(\boldsymbol{x}, t, \boldsymbol{v})$, which denotes the probability of finding, within an infinitesimal spatial element $\mathrm{d}\boldsymbol{x}$ at position $\boldsymbol{x}$ and during the time interval $(t, t + \mathrm{d}t)$, a number of particles whose velocities lie in $(\boldsymbol{v}, \boldsymbol{v} + \mathrm{d}\boldsymbol{v})$. The Boltzmann equation is solved by discretizing the velocity space into a specified set of magnitudes and directions. For low-subsonic flow simulations, the D3Q19 lattice model is

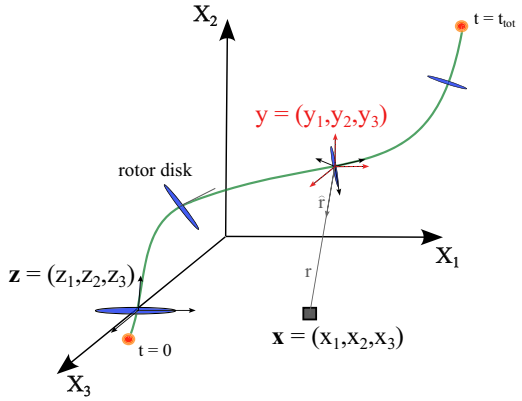


Fig. 4 Generic rotor trajectory. x: global reference frame, z: blade-based reference frame, y: rotor-based reference frame.

commonly adopted, using 19 discrete velocity vectors in three spatial dimensions [32]:

$$f_i(\boldsymbol{x} + \boldsymbol{v}_i\Delta t, t + \Delta t) - f_i(\boldsymbol{x}, t) = C_i(\boldsymbol{x}, t) \tag{10}$$

Here, f_i denotes the particle distribution function associated with the ith discrete velocity direction ($\boldsymbol{v}_i, i = 0, \ldots, 18$). The quantities $\boldsymbol{v}_i\Delta t$ and Δt represent the spatial and temporal increments, respectively. In Eq. (10), the collision term C_i is modeled using the Bhatnagar-Gross-Krook approximation [32]. The LBM discretization is executed on a Cartesian mesh composed of cubic control volumes ("voxels"). Solid boundaries are embedded via planar surface facets ("surfels") constructed within voxels intersecting the geometry. To impose wall boundary conditions, a particle bounce-back scheme and a specular reflection scheme are employed, corresponding to no-slip and slip boundaries, respectively [33]. For rotating elements, the computational domain is split into an outer inertial (ground-fixed) frame and an inner body-fixed Local Reference Frame (LRF). The LRF mesh rotates as a rigid body with the component, thereby removing any relative motion between the rotating grid and the contained geometry. An external body-force term, representing the inertial force arising from the noninertial rotating LRF, is added to the right-hand side of the discrete Boltzmann equation within the LRF fluid region [34]. A closed, transparent interface links the inner and outer domains, ensuring continuity between the two fluid regions. A complete and detailed description of the high-fidelity solver is out of the scope of this work. A more detailed description of the methodology can be found in [32,33,35].

Finally, given the body geometry, kinematics, and surface pressure distribution, the far-field noise is evaluated using the FW-H acoustic analogy, implemented in the PowerACOUSTICS module, based on a forward-time solution. In the present work, the FW–H analogy is applied on impermeable surfaces coincident with the blade geometry, consistently with the LF formulation based on blade resolved loads. Moreover, for the low tip Mach numbers considered here, volumetric quadrupole contributions are expected to be secondary compared to monopole and dipole terms. The accuracy of this methodology, in particular for rotorcraft applications, can be found in many works, such as [36,37,38].

III. Numerical Setup

The high-fidelity computational domain, presented in Fig. 5, is a cube with side length $L = 100D_{\text{prop}}$. The propeller is placed at the domain center. Spatial discretization employs 16 Variable-Resolution (VR) blocks, labeled VR_0-VR_{15}, with grid resolution progressively refined from the outermost region toward the region of interest surrounding the propeller, with the smallest voxel size equal to 7.8125e − 05 m. The grid resolution changes with a factor two between adjacent VR regions. As resolving the near-wall region with $y^+ < 1$ is computationally infeasible, the propeller surface is modeled

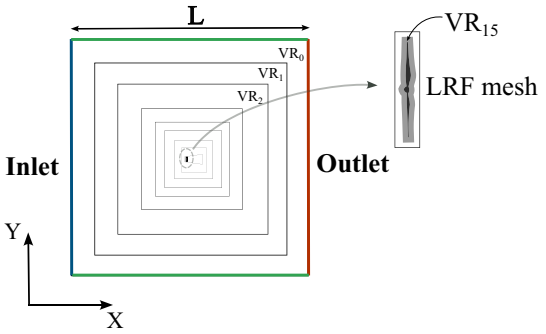


Fig. 5 High-fidelity computational domain. The LRF mesh rotates with the propeller. Velocity and pressure boundary conditions are prescribed at the inlet and outlet, respectively.

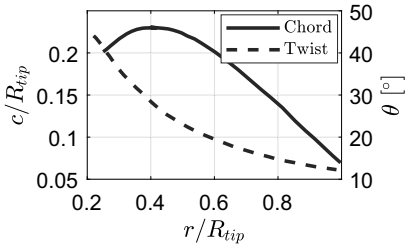


Fig. 6 Propeller nondimensional chord (c/R_{tip}) and twist θ distributions along the nondimensional radial distance (r/R_{tip}).

using a fully turbulent wall-function formulation that incorporates pressure-gradient effects [39].

The blade used for the simulations in the same already used in [6] and [36]; it is a 2 bladed-propeller with $D = 0.3$ m, with NACA-4412 airfoils. The twist (θ) and chord distribution of the blade along its radius is shown in Fig. 6.

Although the high-fidelity configuration is relatively elaborate, the low-fidelity setup is straightforward because no mesh is needed. Only a small set of inputs is required to reconstruct the blade: geometric distributions (chord, twist, height, sweep) along the propeller radius, airfoils, hub-to-tip ratio, and the propeller diameter. After the blade is reconstructed, the number of blade elements N_b for discretization is specified, followed by the operating conditions.

IV. Validation

To assess the accuracy and reliability of the proposed LF framework, its aerodynamic and acoustic predictions are compared against high-fidelity (HF) results available in the literature. The comparison focuses on both aerodynamic performance and tonal noise characteristics of the small-scale two-bladed propeller operating in axial and nonaxial inflow conditions. The selected reference data are taken from previous LB simulations and experimental measurements reported in [6,36]. The propeller geometry adopted in this work is identical to that used in those studies, ensuring direct comparability of the results.

A. Axial-Inflow

First of all, the aerodynamic performance, in terms of thrust coefficient C_T, torque coefficient C_Q, and propulsive efficiency η of the propeller, reported in Eq. (11), for different advance ratios J (where $J = V_\infty/(nD_{\text{prop}})$), with n denoting the revolution per seconds, are compared with the experimental results in [36] for an axial inflow condition, that is a condition in which the freestream velocity vector V_∞ is parallel to the rotational axis of the propeller ($\alpha = 0$ deg). For the LF simulations, a number of blade elements $N_b = 15$ has been selected. The total number of revolutions N_{rev} has been set to 10, ensuring convergence of the aerodynamic coefficients and full development of the wake, with a time step $\text{d}t = 1.65\text{e} - 4$ s, corresponding to 5 deg of rotation per time step:

$$C_T = \frac{T}{\rho_\infty n^2 D_{\text{prop}}^4} \quad C_Q = \frac{Q}{\rho_\infty n^2 D_{\text{prop}}^5} \quad \eta = J\frac{C_T}{C_Q} \tag{11}$$

As can be seen in Fig. 7, the aerodynamic coefficients computed by the aerodynamic solver match quite well with the experimental results from [36]. At low advance ratios, the thrust coefficient is overpredicted, while at higher advance ratios it is underpredicted. In contrast, the torque coefficient is underpredicted by about 7% at low advance ratios, a behavior that is consequently mirrored in the propulsive efficiency.

The HF results in [6] are used for comparison of the far-field noise. Figure 8 shows the thickness and loading noise, for the single propeller, in axial inflow, with $J = 0.4$ and constant angular velocity equal to 5000 rpm. The SPL directivity is computed in a plane perpendicular to the propeller plane and the sampling points are located at a distance of ten times the radius of the propeller ($R = 10R_{\text{tip}}$). The LF results matches well with the HF results. Maximum differences are on the order of 3 dB for $\Theta = 30$ deg, for the loading noise, while they are negligible for the thickness noise.

B. Nonaxial Inflow

A more challenging condition is represented by a nonaxial inflow, in which the freestream vector is inclined with respect to the propeller axis by an angle α. This regime causes an unsteady relative velocity, which significantly affects the SPL directivity. In Fig. 9, the ratio between the sectional thrust and torque coefficient per unit span, expressed in Eq. (12), in the nonaxial inflow ($\alpha = 15$ deg) with respect to the axial inflow ($\alpha = 0$ deg) condition, for a fixed blade radial position $r/R_{\text{tip}} = 0.5$, is shown as a function of the azimuthal position Ψ of the blade during its rotation:

$$C_{\partial rT} = \frac{\partial T/\partial r}{\rho_\infty n^2 D_{\text{prop}}^3} \quad C_{\partial rQ} = \frac{\partial Q/\partial r}{\rho_\infty n^2 D_{\text{prop}}^4} \tag{12}$$

The results computed with FLOWUnsteady are in agreement with the high-fidelity data from [6]. More in detail, when the free-stream velocity is inclined relative to the propeller axis, both the thrust and torque distributions along the blade sections vary periodically with the blade's azimuthal position, reaching their maximum and minimum values for azimuth angles of $\psi = 90$ and 270 deg, respectively.

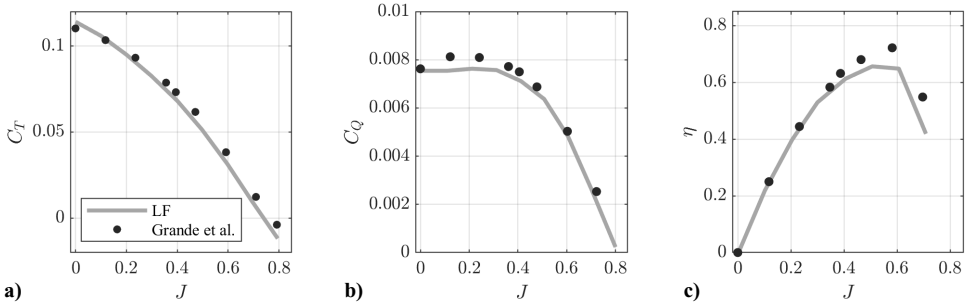


Fig. 7 Aerodynamic performance comparison for $\alpha = 0$ deg and $\Omega = 5000$ rpm. LF results are compared with [36].

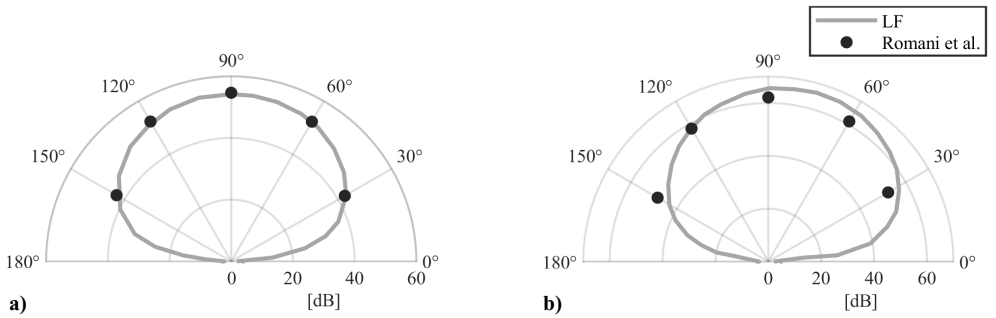


Fig. 8 SPL (I BPF) directivity comparison for $J = 0.4$. Thickness noise a) and loading noise b), for $\alpha = 0$ deg. LF results are compared with [6].

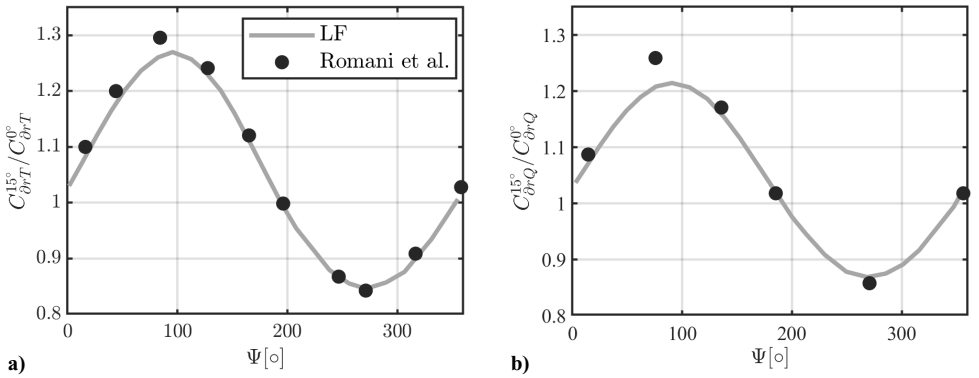


Fig. 9 Comparison of ratio of the thrust a) and torque b) coefficients between $\alpha = 15$ and 0 deg cases for a spanwise location equal to $r/R_{\text{tip}} = 0.5$, for $J = 0.4$. LF results are compared with [6].

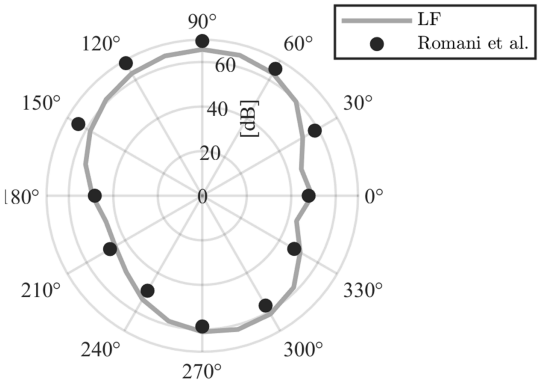


Fig. 10 SPL (I BPF) comparison for $J = 0.4$ and $\alpha = 15$ deg. LF results are compared with [6].

For $\alpha = 15$ deg, the increase in sectional thrust and torque coefficients on the blade advancing side is greater than the corresponding reductions on the retreating side. This behavior is mainly due to the greater increase in the local airfoil angle of attack, caused by an increase in tangential velocity on the advancing side compared to the decrease occurring on the retreating side.

Observing Fig. 10, the noise directivity loses its symmetry, together with a substantial increase in SPL along the propeller axis with respect to the axial-inflow case. This change in directivity can be attributed to the modification of loading noise for $\alpha = 15$ deg, caused by the unsteadiness of the blade loading during the propeller rotation, in agreement with the behavior of the blade loading as a function of azimuthal position of the blade shown in Fig. 9.

Overall, the comparisons demonstrate that the LF framework provides an accurate prediction of both aerodynamic and acoustic quantities when compared against high-fidelity and experimental results available in the literature. This validation is intended as a preliminary step, ensuring the consistency of the proposed approach before extending the analysis to more complex unsteady operating conditions, as discussed in the following section.

V. Results

In this section, the aerodynamic characteristics and far-field noise of a single propeller subjected to an angular velocity variation are analyzed. Two numerical approaches are employed: the LF framework previously described and the HF approach based on the LB/VLES simulation method implemented in the commercial software PowerFLOW®.

The analysis is structured in two parts. First, a steady uniform inflow condition is considered for an isolated rotor with the same geometry described in the previous sections. This preliminary study serves to validate and justify the numerical setup adopted in the subsequent transient case. Moreover, the steady operating point is introduced as a baseline to ensure consistency between LF and HF at the initial condition of the transient. Then, a short angular velocity transient is investigated to assess the LF framework performance in unsteady operating conditions and its impact on the far-field noise.

A. Steady Conditions

In this section, the aerodynamic and aeroacoustic performance of a single propeller operating under steady conditions is analyzed, i.e. constant angular velocity. The inflow velocity V_∞ is uniform and constant at 3 m/s, while the angular velocity Ω is kept constant at 5000 rpm, resulting in $J = 0.12$. For the LF approach, the same numerical setup and simulation parameters described in the previous section are adopted. The HF configuration follows the setup presented in Sec. III, which has also been presented in previous works [5,6].

Figure 11 shows the dimensionless thrust and torque distributions along the propeller radius. The LF results follow the same trend as the HF predictions, except for the torque near the blade tip. The underestimation observed in the LF approach may be attributed to the application of the Prandtl tip-loss correction implemented in the aerodynamic solver. This discrepancy is reflected in the overall torque coefficient (C_Q), as summarized in Table 1.

Regarding the aeroacoustic analysis, the sound pressure is sampled on a circular array of radius $R = 10R_{\text{tip}}$ located in the X–Z plane, perpendicular to the propeller disk and intersecting the hub centerline ($Y = 0$), as shown in Fig. 12.

Figure 13 compares the acoustic pressure signals predicted by the HF and LF solvers at two azimuthal positions, $\Theta = 90$ and 45 deg, the HF and LF waveforms exhibit good agreement with HF results both in phase and amplitude. The HF results show slightly larger amplitudes because of the broadband noise which is not modeled in the LF approach. The broadband noise becomes dominant approaching the propeller axis, as can be seen in the acoustic

Table 1 Performance coefficients for $J = 0.12$

Coeff.	HF	LF	ϵ, %
C_T	0.1156	0.1147	0.78
C_Q	0.0093	0.0089	3.53

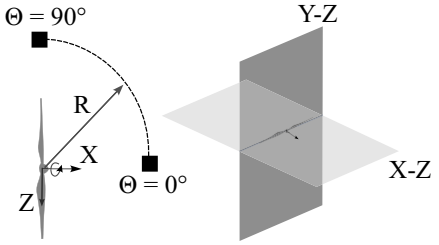


Fig. 12 Microphone array, $R = 10R_{\text{tip}}$.

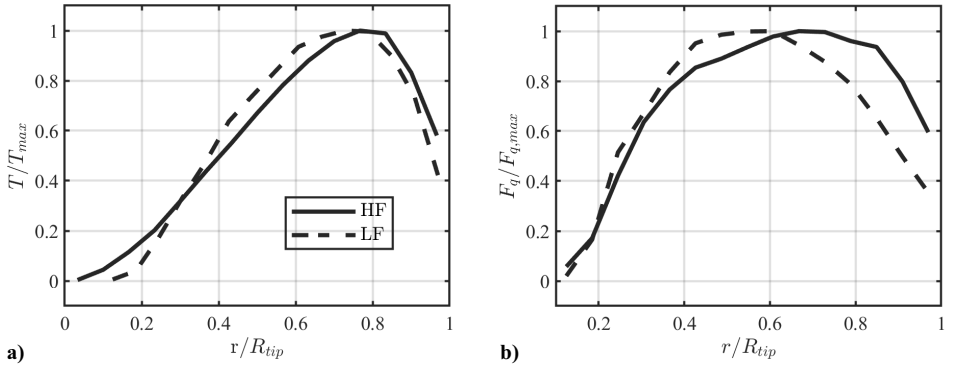


Fig. 11 Dimensionless thrust a) and torque b) distributions comparison along the blade radius for $J = 0.12$ (steady condition).

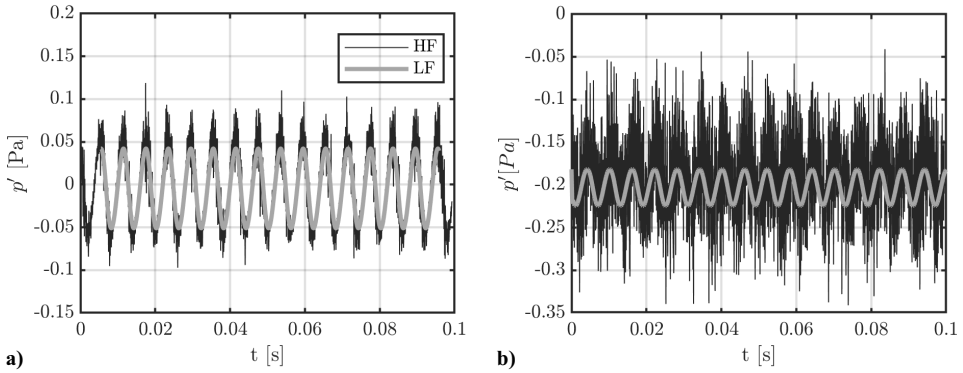


Fig. 13 Acoustic pressure comparison at two azimuthal positions, a) $\Theta = 90$ deg and b) $\Theta = 45$ deg, for $J = 0.12$ (steady condition).

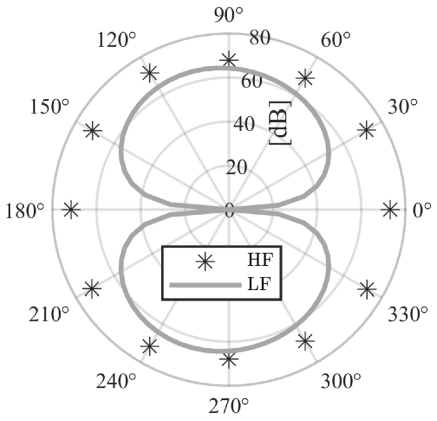


Fig. 14 OASPL directivity comparison for $J = 0.12$ (steady condition).

pressure signal for $\Theta = 45$ deg, and in the Overall Sound Pressure Level directivity of Fig. 14.

Since the LF framework is restricted to tonal noise (thickness and loading contributions), broadband noise components are not modeled. Therefore, comparisons between LF and HF results are performed by focusing on discrete tonal components at the blade-passing frequency (BPF) and its harmonics, obtained through phase-averaging of the pressure signals.

Focusing on the tonal contribution, Fig. 15 presents the SPL directivity patterns corresponding to the first three blade-passing frequencies (BPF I–III), comparing results from the HF and LF solvers, obtained after phase-averaging the pressure signals to isolate the discrete tonal components. For all three BPFs, the LF predictions capture the main features of the HF directivity patterns, particularly the orientation and amplitude of the main lobes. Some discrepancies are observed in the side-lobe regions and near the rotor axis, where the LF model tends to underpredict the SPL levels.

Since broadband noise has been filtered out from the HF results, the remaining differences are attributed to the increased sensitivity of higher-order harmonics to the detailed temporal and spatial structure of the acoustic sources, which are only partially represented in the low-fidelity formulation. As the BPF order increases, the radiation pattern becomes more directional, with higher SPL values concentrated near the axial direction.

The corresponding spectral distributions, reported in Fig. 16 for several azimuthal positions, further highlight the tonal and broadband characteristics of the two approaches. The LF spectra display distinct peaks at the BPF and its harmonics, reflecting the tonal nature of the modeled noise. In contrast, the HF spectra include both these discrete components and a broadband contribution extending over a wide frequency range. The broadband content is more pronounced in the axial direction (e.g., $\Theta = 210$ and 30 deg), suggesting a stronger influence of turbulent flow features and secondary sources in those regions. Despite these additional components, the LF model consistently captures the dominant tone, usually associated to the steady loading, across all observer angles, confirming its capability to reproduce the principal periodic features of the radiated sound field with significantly reduced computational cost.

B. Transient Angular Velocity

In this section, the effect of an angular velocity transient on tonal noise is investigated. A linear angular velocity increase between two steady-state conditions is considered. The rotor geometry is the same as previous. The angular velocity varies linearly from 5000 ($J = 0.12$) to 6000 rpm ($J = 0.1$) over a transient period (Δt) of 0.1 s, with a constant inflow velocity of 3 m/s. During the angular velocity transient, both thrust and torque increase, as shown in Fig. 17, where the HF and LF results exhibit good agreement. The rise in thrust and torque is accompanied by a corresponding increase in amplitude of the acoustic pressure fluctuations. Figure 18 presents the time evolution of the acoustic pressure during the transient phase (0.2–0.3 s) for two azimuthal positions. As observed under steady conditions, the LF solver underestimates the acoustic pressure compared to the HF solver. This discrepancy becomes more pronounced near the propeller axis, where broadband noise dominates.

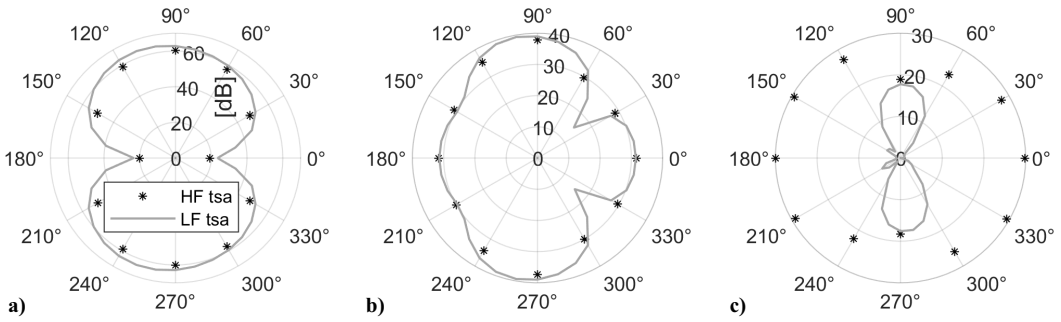


Fig. 15 SPL directivity comparison for the a) first, b) second, and c) third BPF, for $J = 0.12$ (time synchronous averaged signals, steady condition).

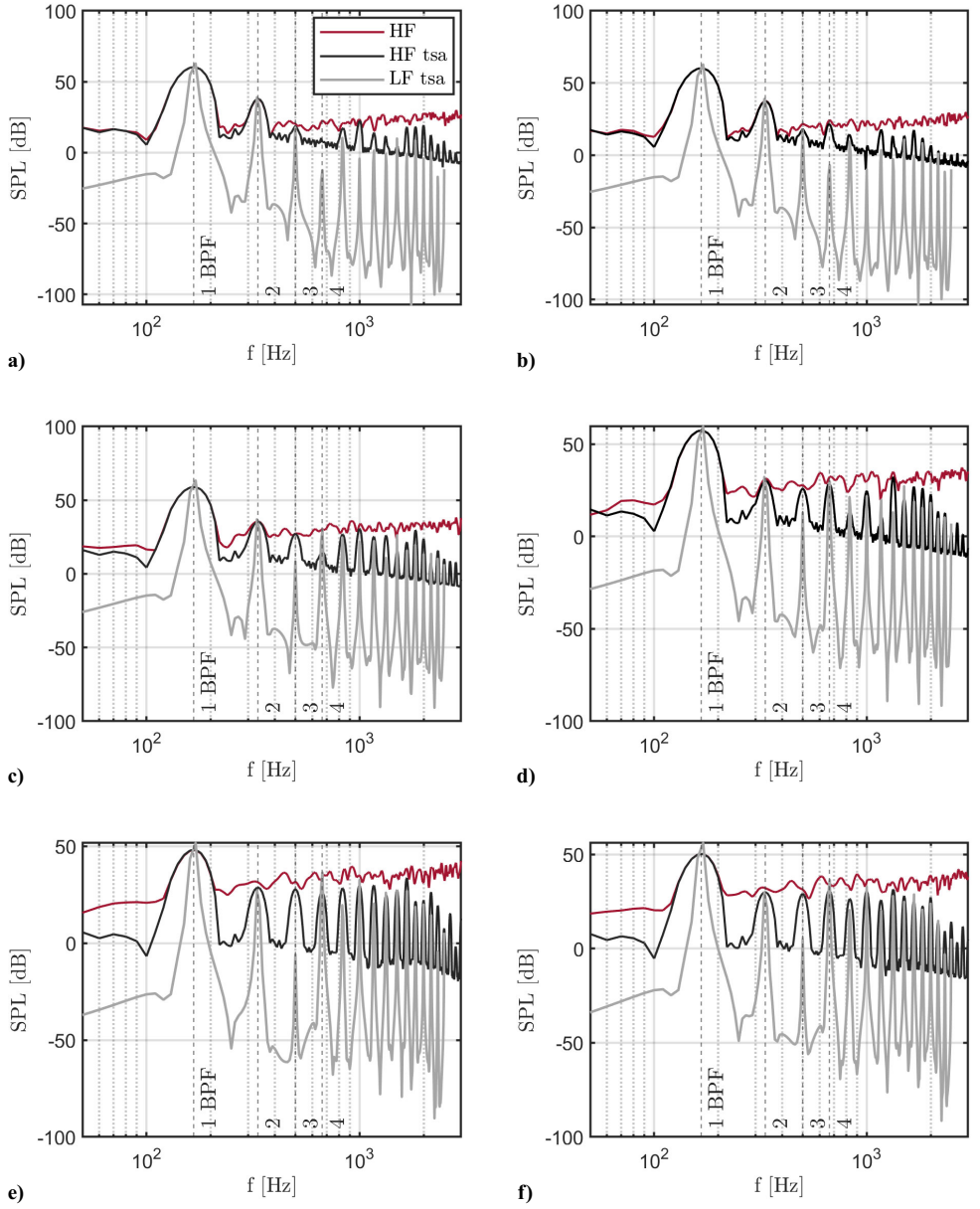


Fig. 16 SPL spectra comparison for the HF, HF time synchronous averaged, and LF time synchronous averaged signals, for $J = 0.12$ (steady condition). a) $\Theta = 90$ deg, b) $\Theta = 270$ deg, c) $\Theta = 120$ deg, d) $\Theta = 300$ deg, e) $\Theta = 30$ deg, and f) $\Theta = 210$ deg.

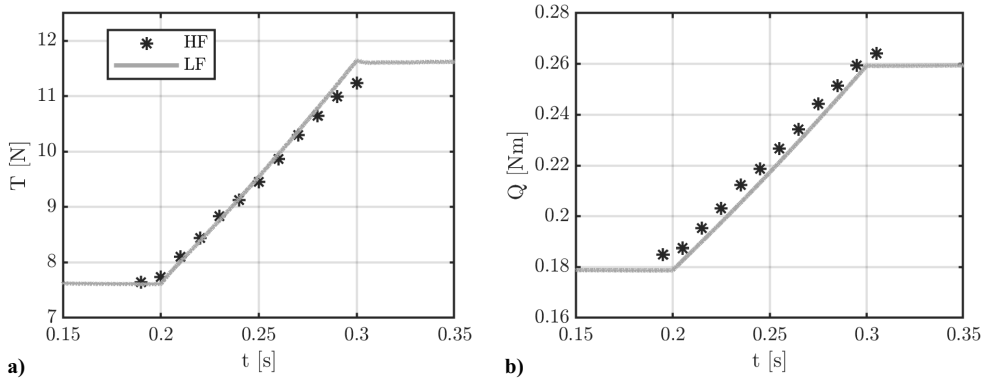


Fig. 17 a) thrust and b) torque during an angular velocity transient (5000–6000 rpm).

Despite the underestimation, the SPL spectrograms in Fig. 19 show that the tonal components display only minor differences between the two solvers. In particular, the I and II BPF follow similar transient dynamics for both in-plane and out-of-plane observers. Furthermore, the $\Theta = 45$ deg spectrogram reveals the emergence of additional high-frequency tones, particularly in the 1000–2000 Hz range, which is not observed for $\Theta = 90$ deg at 5000 rpm.

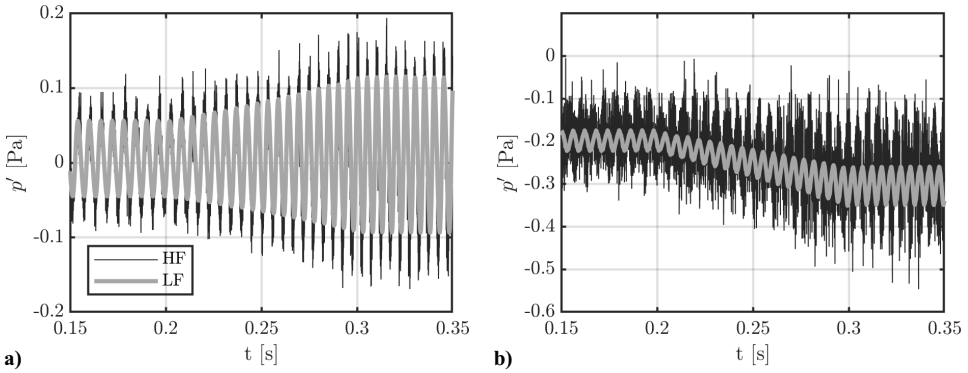


Fig. 18 Acoustic pressure comparison at two azimuthal positions a) $\Theta = 90$ deg and b) $\Theta = 45$ deg, transient angular velocity (5000–6000 rpm).

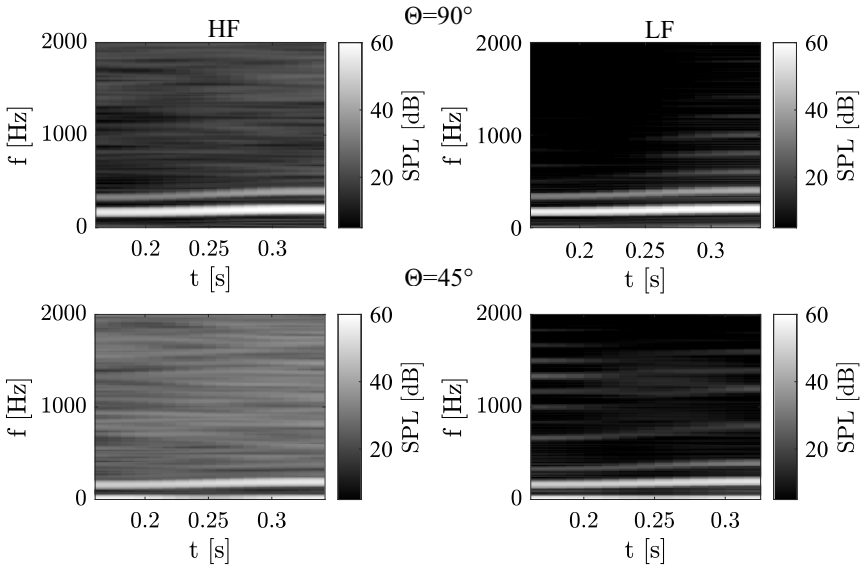


Fig. 19 SPL spectrograms at two azimuthal positions ($\Theta = 90$ deg and $\Theta = 45$ deg), transient angular velocity (5000–6000 rpm).

A pronounced low-frequency component is observed close to the rotor axis, as can be seen in the spectrograms of Fig. 19. This behavior is associated with the thrust contribution, which becomes dominant in the radiation force F_r, expressed in Eq. (9), and observable in Fig. 20. Since the thrust primarily radiates along the rotor axis (corresponding to the F_x component in Fig. 20), its acoustic influence is negligible in the rotor plane ($\Theta = 90$ deg). Conversely, for observers located at intermediate polar angles (e.g. $\Theta = 45$ deg), the axial thrust component contributes significantly to F_r, leading to a nonzero, slowly varying mean value of the pressure signal. As a result, while the pressure waveform at $\Theta = 90$ deg exhibits an approximately zero mean, a varying nonzero mean emerges at $\Theta = 45$ deg, giving rise to the observed low-frequency content.

The behavior of the radiation force F_r is reflected in the SPL time-history. Figure 21 (right) shows the temporal variation of the SPL directivity during the transient. Near the disk plane ($\theta = 90$ and 270 deg), the SPL varies smoothly between the two steady conditions, gradually increasing over time. In contrast, for observers located near the propeller axis ($\theta = 0$ and 180 deg), a sharp SPL rise occurs during the transient phase (0.2–0.3 s). Additionally, an overshoot in SPL is observed at both the beginning and the end of the transient.

To better assess the influence of time-varying aerodynamic forces and their derivatives, the SPL time-history at $\Theta = 10$ deg is presented in Fig. 21 (left). The two curves, where "ND" indicates the condition with forcing $\dot{F} = 0$ in Eq. (9), show similar overall trends.

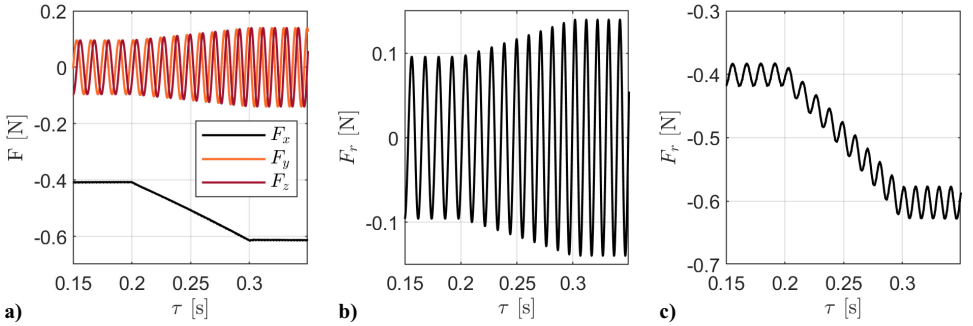


Fig. 20 Force acting on a single blade element ($r/R = 0.75$) during transient angular velocity (5000–6000 rpm). a) force acting in the global reference frame, b) force acting in the radiation direction for $\Theta = 90$ deg, and c) $\Theta = 10$ deg, as a function of emission time τ.

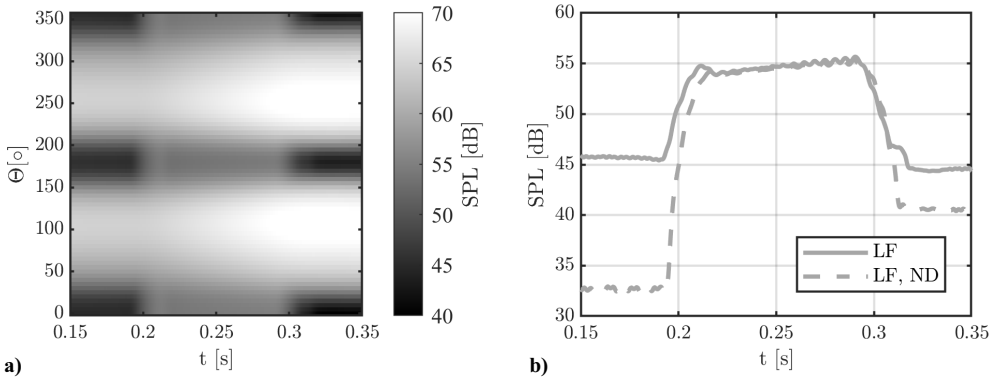


Fig. 21 a) SPL directivity and b) time-varying SPL for $\Theta = 10$ deg. ND: $\dot{F} = 0$.

In both steady states, the SPL remains constant, whereas it rapidly increases at the onset of the transient, then slightly rises throughout the transient, and finally decreases as the transient ends. In the ND case, the absence of the overshoot confirms that this effect is caused by the time derivative of the aerodynamic force, while the rapid SPL increase during the transient is linked to the linear variation of the mean acoustic pressure superimposed on the fluctuations, as observed in the acoustic pressure signals, and highlighted in previous works [22,20].

The increase in SPL observed during the transient phase, caused by the variation of the mean acoustic pressure, follows the assigned transition law, which governs the evolution of the rotor forces and, consequently, the pressure signal. In the previous case, the mean acoustic pressure varied linearly with time, resulting in a constant SPL shift between the two steady conditions. To further support this interpretation, a different transition law between two steady states at 4000 ($J = 0.15$) and 5000 rpm ($J = 0.12$) is considered. Equation (13) defines an error-function-based transition, where the parameter a controls the transient duration: the larger the a, the shorter the transition time between the two steady conditions:

$$\Omega = 4000 + 1000 \cdot \frac{\mathrm{erf}[(t - 0.5)a] + 1}{2} \tag{13}$$

Figure 22 compares the SPL obtained using two transition rates, with $a = 40$ (corresponding to $\Delta t = 0.1$ s) and $a = 10$ (corresponding to $\Delta t = 0.5$ s). The figure clearly shows that the SPL increase during the transient is directly related to the transition law, reaching its peak when the first time derivative of the function is maximum. Furthermore, it is evident that the SPL amplification becomes more pronounced as the transient time decreases, indicating a strong dependence of the acoustic response on the rate of change of the rotor speed.

VI. Conclusions

A low-fidelity framework for rotor noise prediction under both steady conditions and rapid angular velocity variations has been implemented and validated against high-fidelity Lattice–Boltzmann simulations. The results demonstrate that the proposed methodology accurately reproduces both aerodynamic and acoustic trends while requiring orders of magnitude less computational effort (few hours compared with days). The low-fidelity solver successfully captures the main tonal noise characteristics, including the blade-passing frequencies and their evolution during time-varying operating conditions.

The analysis of a short angular velocity transient highlights a strong correlation between the variation of mean acoustic pressure and the imposed transition law governing the rotor speed. The SPL time-history follows the rate of change of the angular velocity, reaching its maximum when the first time derivative of the transition function peaks. Furthermore, a pronounced low-frequency component appears near the rotor axis, associated with the axial loading and quasi-steady pressure field induced by the thrust variation that increases considerably the SPL during the transient, which is not captured in a quasi-steady approach.

Comparison with high-fidelity results confirms that the low-fidelity framework can reliably predict both steady and transient tonal noise, capturing the main physical mechanisms driving the acoustic response. The method's efficiency and robustness make it a valuable tool for preliminary noise assessments of distributed-propulsion systems and eVTOL architectures under maneuvering conditions and pave the way for future perception-oriented noise studies of propeller-based configurations under transient operating conditions through the proper integration of psychoacoustic metrics. It is finally noted that the present work does not include a direct validation against new experimental acoustic measurements. Instead, high-fidelity simulations are used as a controlled reference, relying on the fact that the same solver and propeller configuration

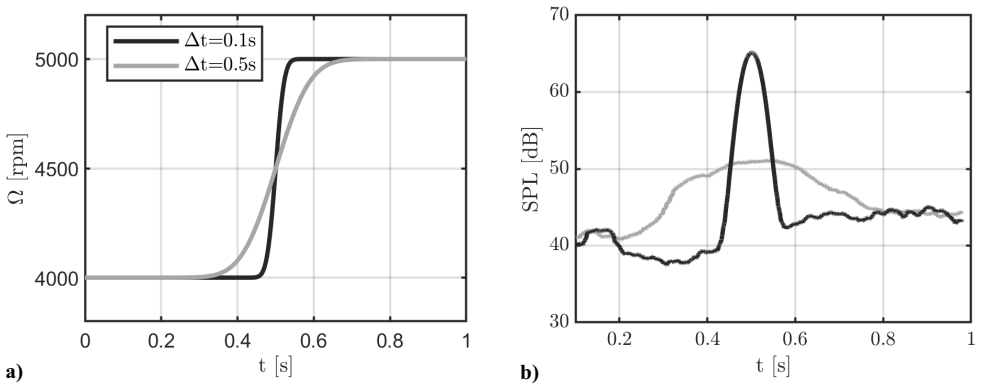


Fig. 22 a) Error function transient (4000–5000 rpm) and b) time-varying SPL for $\Theta = 10$ deg.

has been extensively validated against experiments in previous studies. This validation strategy introduces an intrinsic limitation, as uncertainties associated with the high-fidelity modeling may affect the comparison. Future work will therefore focus on dedicated experimental campaigns, particularly under transient rotor operating conditions, for which high-quality acoustic datasets are currently scarce.

Acknowledgments

This publication is part of the project PNRR-NGEU, which has received funding from the MUR-DM 117/2023, and is co-funded by the Italian Aerospace Research Center (CIRA).

References

[1] Zhou, Y., Zhao, H., and Liu, Y., "An Evaluative Review of the VTOL Technologies for Unmanned and Manned Aerial Vehicles," *Computer Communications*, Vol. 149, 2020, pp. 356–369. https://doi.org/10.1016/j.comcom.2019.10.016

[2] Hasan, S., "Urban Air Mobility (UAM) Market Study," Tech. Rept. NASA, 2018.

[3] Jamaluddin, N. S., Celik, A., Baskaran, K., Rezgui, D., and Azarpeyvand, M., "Aerodynamic Noise Analysis of Tilting Rotor in Edgewise Flow Conditions," *Journal of Sound and Vibration*, Vol. 582, 2024, Paper 118423. https://doi.org/10.1016/j.jsv.2024.118423

[4] Voropayev, V., Marques, M., Maleki, A., Grace, S., Lyrintzis, A. S., Mankbadi, R. R., and Golubev, V. V., "High-Fidelity Simulations of Vertiport Gust Effects on eVTOL Rotor Noise," *AIAA Aviation Forum*, AIAA Paper 2025-3001, 2025. https://doi.org/10.2514/6.2025-3001

[5] Alı, M., Piccolo, A., Zamponi, R., Ragni, D., and Avallone, F., "On the Impact of Turbulent Inflow on the Noise Generated by a Propeller Operating at Low Reynolds Number," *Forum Acusticum*, 2025.

[6] Romani, G., Grande, E., Avallone, F., Ragni, D., and Casalino, D., "Computational Study of Flow Incidence Effects on the Aeroacoustics of Low Blade-Tip Mach Number Propellers," *Aerospace Science and Technology*, Vol. 120, 2022, Paper 107275. https://doi.org/10.1016/j.ast.2021.107275

[7] Song, P. W., Han, H. Z., Avallone, F., and Qiao, D. Z., "Prediction of Hovering Rotor Noise Based on Reynolds-Averaged Navier–Stokes Simulation," *Journal of Aircraft*, Vol. 44, No. 4, 2007, pp. 1391–1395. https://doi.org/10.2514/1.28310

[8] Yangzhou, J., Wu, J., Ma, Z., and Huang, X., "Aeroacoustic Sources Analysis of Wake-Ingesting Propeller Noise," *Journal of Fluid Mechanics*, Vol. 962, 2023, Paper A29. https://doi.org/10.1017/jfm.2023.295

[9] Schulten, J. B. H. M., "Frequency-Domain Method for the Computation of Propeller Acoustic," *AIAA Journal*, Vol. 26, No. 9, 1988, pp. 303–304. https://doi.org/10.2514/3.10008

[10] Succi, G. P., Munro, D. H., and Zimmer, J. A., "Experimental Verification of Propeller Noise," *AIAA Journal*, Vol. 20, No. 11, 1982, pp. 1–13. https://doi.org/10.2514/3.51211

[11] Boots, D., and Feszty, D., "Numerical Investigation of the Effect of Wing Position on the Aeroacoustic Field of a Propeller," *52nd AIAA/SAE/ASEE Joint Propulsion Conference*, 2016. https://doi.org/10.2514/MJPC16

[12] Hanson, D. B., "Helicoidal Surface Theory for Harmonic Noise of Propellers in the Far Field," *AIAA Journal*, Vol. 18, No. 10, 1980, pp. 1213–1220. https://doi.org/10.2514/3.50873

[13] Farassat, F., "Derivation of Formulations 1 and 1A of Farassat," Tech. Rept., NASA, 2007.

[14] Bergmann, O., Mohren, F., Braun, C., and Janser, F., "Comparison of Various Aeroacoustic Propeller Noise Prediction Methodologies in Static Operations," *AIAA SciTech Forum*, AIAA Paper 2022-2529, 2022. https://doi.org/10.2514/6.2022-2529

[15] Hambrey, J., Kotwicz Herniczek, M. T., Feszty, D., Meslioui, S., and Park, J., "Comparison of Three Popular Methods for the Prediction of High Speed Propeller Noise," *23rd AIAA/CEAS Aeroacoustics Conference*, AIAA Paper 2017-4181, 2017. https://doi.org/10.2514/6.2017-4181

[16] Sharma, A., and Chen, H., "Prediction of Aerodynamic Tonal Noise from Open Rotors," *Journal of Sound and Vibration*, Vol. 332, No. 16, 2013, pp. 3832–3845. https://doi.org/10.1016/j.jsv.2013.02.027

[17] Kvurt, A., and Stalnov, O., "From the Blade Geometry to Prediction of Tonal Noise Component in Hover," *28th AIAA/CEAS Aeroacoustics 2022 Conference*, AIAA Paper 2022-3076, 2022. https://doi.org/10.2514/6.2022-3076

[18] Yunus, F., Grande, E., Casalino, D., Avallone, F., and Ragni, D., "Efficient Low-Fidelity Aeroacoustic Permanence Calculation of Propellers," *Aerospace Science and Technology*, Vol. 123, 2022, Paper 107438. https://doi.org/10.1016/j.ast.2022.107438

[19] Monteiro, F., Ragni, D., Avallone, F., and Sinnige, T., "Low-Order Acoustic Prediction Tool for Estimating Noise Emissions from Distributed Propeller Configurations," *AIAA AVIATION 2023 Forum*, AIAA Paper 2023-4180, 2023. https://doi.org/10.2514/6.2023-4180

[20] Bres, G. A., Brentner, K. S., Perez, G., and Jones, H. E., "Maneuvering Rotorcraft Noise Prediction," *Journal of Sound and Vibration*, Vol. 275, Nos. 3–5, 2004, pp. 719–738. https://doi.org/10.1016/j.jsv.2003.07.005

[21] Chen, H. N., Brentner, K. S., Lopes, L. V., and Horn, J. F., "An Initial Analysis of Transient Noise in Rotorcraft Maneuvering Flight," *International Journal of Aeroacoustics*, Vol. 5, No. 2, 2006, pp. 109–138. https://doi.org/10.1260/147547206777629853

[22] Brentner, K. S., and Farassat, F., "Modeling Aerodynamically Generated Sound of Helicopter Rotors," *Progress in Aerospace Sciences*, Vol. 39, Nos. 2–3, 2003, pp. 83–120. https://doi.org/10.1016/S0376-0421(02)00068-4

[23] Bergmann, O., Mohren, F., Braun, C., and Janser, F., "Propeller Noise Prediction for Transient eVTOL Missions," *AIAA SCITECH 2024 Forum*, AIAA Paper 2024-2636, 2024. https://doi.org/10.2514/6.2024-2636

[24] McKay, R., and Kingan, J. M., "Multirotor Unmanned Aerial System Propeller Noise Caused by Unsteady Blade Motion," *AIAA/CEAS Aeroacoustics Conference*, AIAA Paper 2019-2499, 2019. https://doi.org/10.2514/6.2019-2499

[25] Alvarez, E. J., and Ning, A., "Development of a Vortex Particle Code for the Modeling of Wake Interaction in Distributed Propulsion," *2018 Applied Aerodynamics Conference*, AIAA Paper 2018-3646, 2018. https://doi.org/10.2514/6.2018-3646

[26] Dassault Systèmes, "*PowerFLOW. Commercial CFD Software*," 2025.

[27] Alvarez, E. J., and Ning, A., "Modeling Multirotor Aerodynamic Interactions Through the Vortex Particle Method," *AIAA Aviation 2019 Forum*, AIAA Paper 2019-2827, 2019. https://doi.org/10.2514/6.2019-2827

[28] Shahjahan, S., Gong, A., Moore, A., and Verstraete, D., "Optimisation of Proprotors for Tilt-Wing eVTOL Aircraft," *Aerospace Science and Technology*, Vol. 144, 2024, Paper 108835. https://doi.org/10.1016/j.ast.2023.108835

[29] Alvarez, E. J., Schenk, A., Critchfield, T., and Ning, A., "Rotor-on-Rotor Aeroacoustic Interactions of Multirotor in Hover," *76th Annual Forum*, Vertical Flight Soc., Fairfax, VA, 2020. https://doi.org/10.4050/F-0076-2020-16489

[30] Glegg, S., and Devenport, W., *Aeroacoustics of Low Mach Number Flows*, Academic Press, Cambridge, MA, 2017.

[31] Yakhot, V., Orszag, S. A., Thangam, S., Gatski, T. B., and Speziale, C. G., "Development of Turbulence Models for Shear Flows by a Double Expansion Technique," *Physics of Fluids A: Fluid Dynamics*, Vol. 4, No. 7, 1992, pp. 1510–1520. https://doi.org/10.1063/1.858424

[32] Chen, H., Chen, S., and Matthaeus, W. H., "Recovery of the Navier–Stokes Equations Using a Lattice-Gas Boltzmann Method," *Physical Review A*, Vol. 45, No. 8, 1992, pp. 5339–5342. https://doi.org/10.1103/PhysRevA.45.R5339

[33] Chen, H., Teixeira, C., and Molvig, K., "Realization of Fluid Boundary Conditions via Discrete Boltzmann Dynamics," *International Journal of Modern Physics C*, Vol. 9, No. 08, 1998, pp. 1281–1292. https://doi.org/10.1142/S0129183198001151

[34] Zhang, R., Sun, C., Li, Y., Satti, R., Shock, R., Hoch, J., and Chen, H., "Lattice Boltzmann Approach for Local Reference Frames," *Communications in Computational Physics*, Vol. 9, No. 5, 2011, pp. 1193–1205. https://doi.org/10.4208/cicp.021109.111110s

[35] Chen, H., Kandasamy, S., Orszag, S., Shock, R., Succi, S., and Yakhot, V., "Extended Boltzmann Kinetic Equation for Turbulent Flows," *Science*, Vol. 301, No. 5633, 2003, pp. 633–636. https://doi.org/10.1126/science.1085048

[36] Grande, E., Romani, G., Ragni, D., Avallone, F., and Casalino, D., "Aeroacoustic Investigation of a Propeller Operating at Low Reynolds Numbers," *AIAA Journal*, Vol. 60, No. 2, 2021, pp. 860–871. https://doi.org/10.2514/1.J060611

[37] Romani, G., and Casalino, D., "Rotorcraft Blade-Vortex Interaction Noise Prediction Using the Lattice-Boltzmann Method," *Aerospace Science and Technology*, Vol. 88, 2019, pp. 147–157. https://doi.org/10.1016/j.ast.2019.03.029

[38] Van der Velden, W., Romani, G., and Casalino, D., "Validation and Insight of a Full-Scale S-76 Helicopter Rotor Using the Lattice-Boltzmann Method," *Aerospace Science and Technology*, Vol. 118, 2021, Paper 107007. https://doi.org/10.1016/j.ast.2021.107007

[39] Romani, G., "Computational Aeroacoustics of Rotor Noise in Novel Aircraft Configurations: A Lattice-Boltzmann Method-Based Study," *Dissertation (tu Delft)*, Delft Univ. of Technology, Delft, The Netherlands, 2022. https://doi.org/10.4233/uuid:5d36b4de-8593-4f7e-bc92-a7ae175a0900